# Communication—Technique for Visualization and Quantification of Lithium-Ion Battery Separator Microstructure

**Marie Francine Lagadec,* Martin Ebner,* Raphael Zahn, and Vanessa Wood[z]**

*Laboratory for Nanoelectronics, ETH Zurich, Zurich CH-8092, Switzerland*

Separators play an important role in lithium-ion battery operation; however, no comprehensive studies of their microstructure and its impact exist. To enable such studies, we present a simple method for separator microstructure visualization and quantification based on focused-ion-beam scanning electron microscopic tomography. Here, we use this approach to visualize a sample of commercial polyethylene separator, calculate its directional effective transport parameters, and explain the impact of these values on battery performance. We further extend this technique to visualize metallic deposition within the separator, which could facilitate the study of lithium plating and dendritic growth.

 [DOI: 10.1149/2.0811606jes] 

Manuscript submitted December 22, 2015; revised manuscript received March 4, 2016. Published March 17, 2016.

Separators in Li-ion batteries (LIBs) prevent electronic contact between positive and negative electrodes while allowing ionic transport between them.[1] In the event of cell failure, separators limit ion transport to avoid internal short-circuiting and thermal runaway.[2] To achieve good transport and suitable mechanical, thermal, and chemical properties, LIB separators are commonly <25 μm-thick sheets consisting of a complex 3D structure featuring 40% porosity and submicron pore sizes.[2] Though they are routinely characterized by thickness, pore size, porosity, as well as thermal and electrical properties,[3] there has been no quantitative measurement of their 3D structure. Microstructural data would be particularly helpful in light of recent studies that link separator structure to the likelihood of LIB failure (e.g., through Li dendrite growth[4]) and changes in separator structure (e.g., through pore closure by mechanical stress and chemical degradation[5,6]) to aging effects in LIBs. Here, we present a simple procedure for visualizing and quantifying separator microstructures. We use simulations to assess the implications of separator microstructure on battery performance and extend our technique to examine lithium metal deposition within the separator.

## Experimental

We employ focused ion beam scanning electron microscopic (FIB-SEM) tomography (Figure S1 in the Supplementary Information[7]), a technique that has been used for visualizing and quantifying of LIB electrode microstructures.[8,9] Figures 1a–1b show top view SEM images of polyethylene (PE) and polypropylene (PP) separators from Targray (PE16A and PP16). SEM images of cross-sectional cuts through the same separators (Figures 1c–1d) taken in the FIB-SEM configuration show pore edge contrast and depth information from the pores. Because these effects complicate image processing and quantification of the 3D microstructure, we in-fill the separator to enable imaging of a planar surface.

Quantification of the 3D microstructure also requires sufficient contrast between the polymer skeleton and the in-filled pores. As a staining agent, we use $OsO_4$,[10] which has previously been used with Celgard microporous membranes[11] as well as lithium dendrites and solid electrolyte interphases of graphite electrodes.[12] PE and PP are inert toward $OsO_4$ staining, but $OsO_4$ reacts with unsaturated C-C double bonds via dihydroxylation.[10,13] As outlined in Figure 1e, we in-fill separator samples with butter,[7] stain with $OsO_4$, and prepare them for FIB-SEM tomographic analysis. Slices of in-filled PE and PP separators are shown in Figures 1f–1g and reveal good contrast between the polymer and pore phases. Comparing the unprocessed (Figures 1f–1g) and binarized (Figures 1h–1i) images shows that the image processing preserves the key structural features.

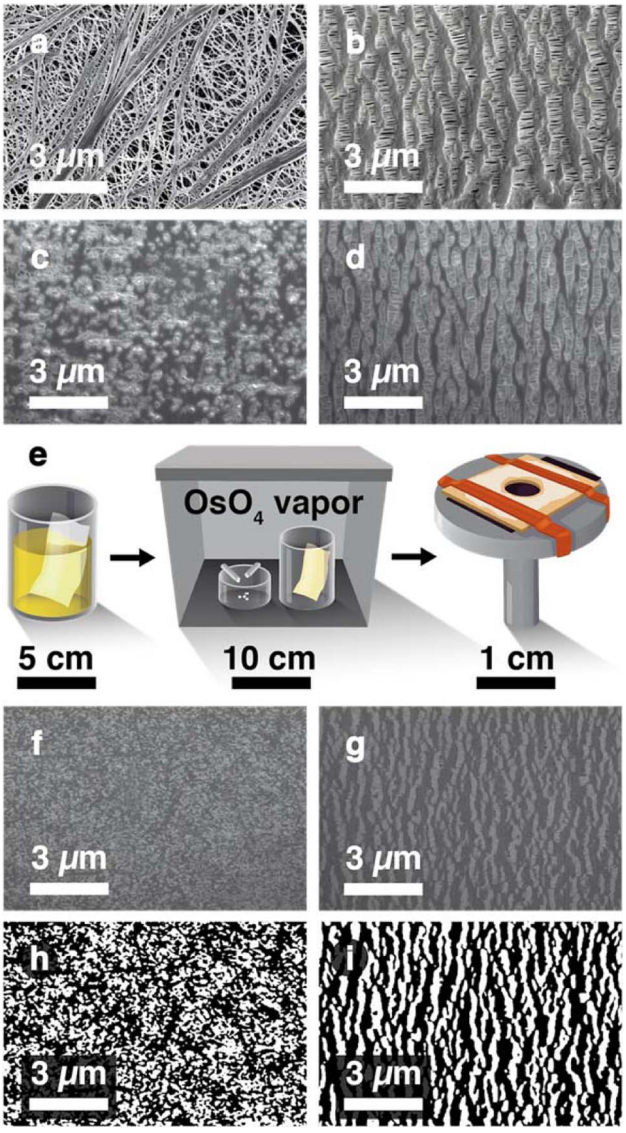


**Figure 1.** Top view SEM images of (a) PE16A and (b) PP16 separator. Cross-section SEM images of (c) PE16A and (d) PP16 separator taken in secondary electron mode. (e) Infilling procedure and FIB-SEM sample preparation for tomographic analysis of in-filled sample. Cross-section SEM images of in-filled (f) PE16A and (g) PP16 separator taken in back-scattered electron mode. Processed cross-section SEM images of in-filled (h) PE16A and (i) PP16 separator.

*Electrochemical Society Student Member.
[z]E-mail: vwood@ethz.ch

**Table I. Mean value μ and standard deviation σ of the microstructural parameter distributions evaluated for the 264 sub-volumes of 2 μm size for the Targray PE16A separator.**

| | | Tortuosity τ [-] | | | Effective transport coefficient δ [-] | | |
|---|---|---|---|---|---|---|---|
| Parameter | Porosity ε [%] | TP | IP1 | IP2 | TP | IP1 | IP2 |
| μ | 40.82 | 2.64 | 2.99 | 2.65 | 0.156 | 0.139 | 0.157 |
| σ | 1.92 | 0.21 | 0.39 | 0.31 | 0.019 | 0.022 | 0.022 |

The binary data set for the PE16A separator is available open source[14] and contains data corresponding to a separator volume of 12 × 7 × 5 $\mu m^3$. Figure 2a presents a rendered sub-volume with an edge length of 2 μm (<1/50th of the total imaged volume). The faces in the through-plane (TP) direction (i.e., the primary direction for ionic transport between the anode and cathode) and the in-plane (IP1 and IP2) directions are shown in Figure 2b.

## Results and Discussion

Our in-filling and staining approach results in stable samples that can be imaged via FIB-SEM tomography with sufficient contrast between the polymer skeleton and pores for straightforward image processing, segmentation, and data reconstruction. As an example of the type of analysis and simulation that can be performed with such 3D structural data, we quantify the microstructure of the PE16A separator and assess its implications on battery performance.

By plotting porosity distributions as a function of sub-volume size (Figure S2a[7]), we can select 2 × 2 × 2 $\mu m^3$ sub-volumes as representative of the entire separator, but providing insight into the local deviations in microstructure parameters. For each of the 264, 8 $\mu m^3$ sub-volumes, we determine the porosity ε, tortuosity τ, and effective transport coefficient $\delta = \varepsilon/\tau$.[15] The mean values μ and standard deviations σ are listed in Table I (see histograms in Figures S2b-c). In agreement with the specified porosity of 40 ± 5% of the PE16A separator, we calculate an ε of 40.82 ± 1.92%. The values τ = 2.64 ± 0.21, 2.99 ± 0.39, and 2.65 ± 0.31 for the TP, IP1 and IP2 directions, respectively, indicate that the PE16A microstructure is quite isotropic. The small differences in the in-plane values can be attributed to wet-stretch manufacturing, which can tend to align the fibrous structure in one direction (Figure 1a). The δ = 0.156 ± 0.019, 0.139 ± 0.022, and 0.157 ± 0.022 for the TP, IP1 and IP2 directions, respectively (Figure 2c), mean that the effective diffusion coefficient $D_{eff}$ for lithium in the separator pore structure is about 14–16% of the diffusion coefficient of Li in the electrolyte $D_0$: $D_{eff} = \delta \cdot D_0$.[15]

COMSOL simulations of an electrolyte soaked separator in a $Li^0$|PE16A|$Li^0$ cell provide insight into how separator microstructure

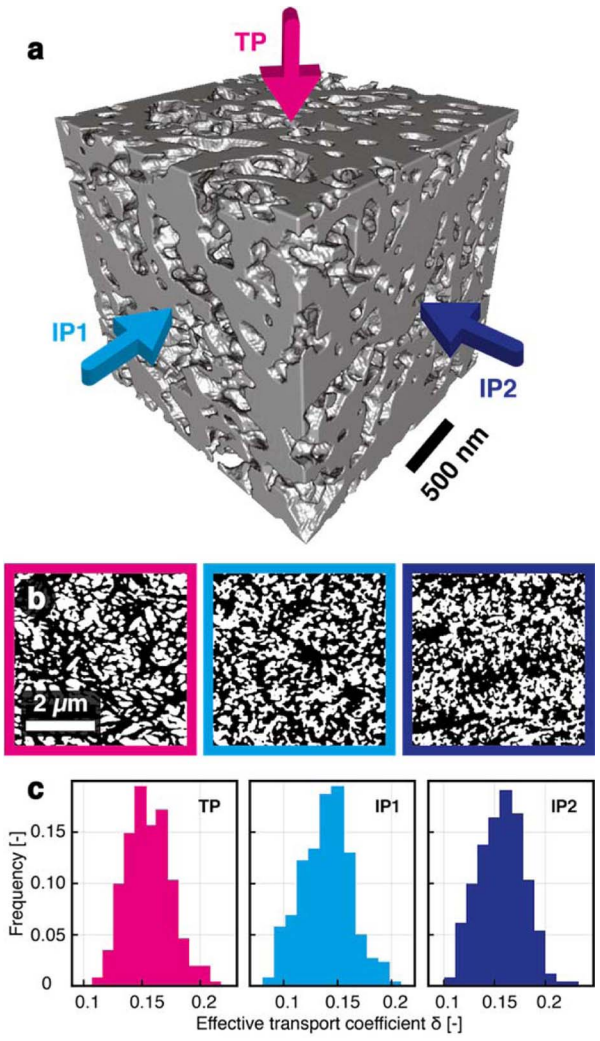


**Figure 2.** (a) 3D microstructure rendering (created with ImageVis3D) of a PE16A separator volume of 2 μm edge length with TP (magenta), IP1 (light blue) and IP2 (dark blue) directions. (b) Binarized SEM images (polymer skeleton in black, pore space in white) of the in-filled PE16A separator in the TP, IP1, and IP2 directions. (c) Effective transport coefficient δ histograms for TP, IP1, and IP2 directions considering 2 μm sub-volumes.

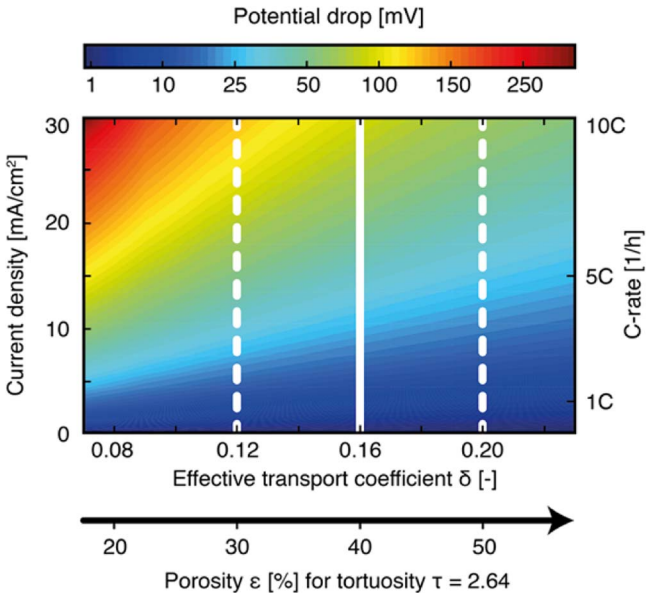


**Figure 3.** Simulated potential drops across separators for different effective transport coefficients δ at varying current densities. The solid and dashed lines indicate the mean δ of the PE16A separator and a 25% lower δ, and 25% higher δ, respectively. This range in δ would occur for example, if tortuosity is fixed at 2.64 and porosity decreases to 30% or increases to 50% (shown on 2nd axis) or if porosity is fixed at 40.82% and tortuosity increases to 3.5 or decreases to 2.1 (not shown). The current density axis (left) is independent of cell chemistry; the C-rate axis (right) indicates how these current densities relate to charging rates for a commercial 3mAh/$cm^2$ graphite electrode.

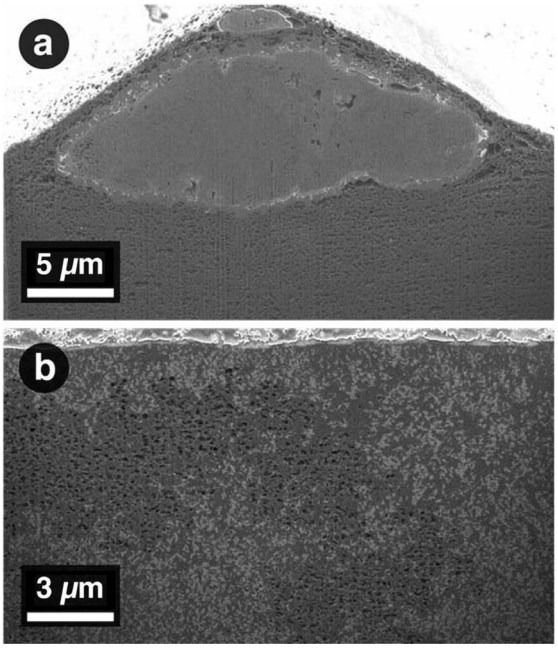


**Figure 4.** Cross-section SEM images of $OsO_4$ stained metallic lithium deposition in PE16A separator from (a) $Li^0$|PE16A|$Li^0$ cell and (b) $Li^0$|PE16A|graphite cell.

influences battery performance.[7] Separator microstructure decreases the electrolyte conductivity and thereby increases the potential drop across the electrolyte-soaked separator. Figure 3 shows that at low current densities, the potential drops across the separator are small and only slightly influenced by variations in δ. However, at high current densities, the potential drops are considerable and highly dependent on separator microstructure. For our PE16A separator with $\delta = 0.16$, we calculate potential drops of 14 mV and 37 mV for applied current densities of 6 and 15 mA/cm$^2$. These current densities correspond to C-rates of 2C and 5C for a typical 3 mAh/cm$^2$ graphite electrode, or 6C and 15C for a typical 1 mAh/cm$^2$ LTO electrode.

Along with the potential drops from the charge transfer resistance and electrolyte resistance in the positive and negative electrodes,[16] the potential drop across the electrolyte in the separator contributes to unwanted effects such as resistive heating. Furthermore, this potential drop must be taken into account in order to properly define cell cut-off voltages and prevent overcharge conditions, which can cause the potential at the electrode to drop below 0 V vs. Li/Li$^+$ and lead to the deposition of lithium metal on the electrode.[17] Our sub-volume analysis shows that while δ varies by more than ±25% in the PE16A separator, this microstructural heterogeneity is on a length scale <4 μm, 1–2 orders of magnitude smaller than the length scale of ∼100 μm for a structural defect to lead to local lithium metal plating on the electrode.[18] This indicates that it is possible to treat the pristine PE16A separator in a macrohomogeneous model, with a single δ describing the impact of separator structure on electrolyte conductivity and diffusivity.

To assess the effect of overcharge, we can use our visualization technique to image metallic lithium deposition that penetrates into the separators. We place PE16A separators harvested from cycled $Li^0$|PE16A|$Li^0$ and $Li^0$|PE16A|graphite cells in a staining container.[7,12] $OsO_4$ reacts with Li, providing contrast between any deposits and the separator structure. The Li structures we image range from micron-sized entities, that deform the separator (Figure 4a), to nanometer sized, separator pore filling metal deposition (Figure 4b). Consistent with the electrochemical data (Figures S3a–b[7]), which does not show evidence for short-circuiting due to dendritic lithium growth, no full penetration of the separator by the lithium structures is observed.

## Summary

We provide the 3D microstructural data of a PE separator open source[14] to encourage future efforts in modeling lithium ion diffusion, heat conduction, or dendrite growth. We hope that this data and the simple approach for visualizing and quantifying the microstructures of LIB separators presented will benefit experimental and computational work aimed at improving separator and battery design.

## Acknowledgments

Funding for the project was provided by an ETH Research Grant, a seed grant from ETH Energy Science Center Seed Fund, and the Gebert Rüf Stiftung. M. F. L. thanks Simon Müller for his support with GeoDict and MATLAB.

## References

1. C. J. Orendorff, *The Electrochemical Society Interface*, 61 (2012).
2. P. Arora and Z. Zhang, *Chem. Rev.*, **104**, 4419 (2004).
3. S. S. Zhang, *J. Power Sources*, **164**, 351 (2007).
4. A. Jana, D. R. Ely, and R. E. García, *J. Power Sources*, **275**, 912 (2015).
5. C. Peabody and C. B. Arnold, *J. Power Sources*, **196**, 8147 (2011).
6. J. Cannarella and C. B. Arnold, *J. Power Sources*, **245**, 745 (2014).
7. See supplementary information at http://dx.doi.org/10.1149/2.0811606jes for additional information.
8. D. E. Stephenson, B. C. Walker, C. B. Skelton, E. P. Gorzkowski, D. J. Rowenhorst, and D. R. Wheeler, *J. Electrochem. Soc.*, **158**, A781 (2011).
9. M. Ender, J. Joos, T. Carraro, and E. Ivers-Tiffée, *J. Electrochem. Soc.*, **159**, A972 (2012).
10. P. Echlin, *Handbook of Sample Preparation for Scanning Electron Microscopy and X-Ray Microanalysis*, p. 137, Springer Science+Business Media, LLC (2009).
11. T. Sarada, L. C. Sawyer, and M. I. Ostler, *J. Membr. Sci.*, **15**, 97 (1983).
12. M. Zier, F. Scheiba, S. Oswald, J. Thomas, D. Goers, T. Scherer, M. Klose, H. Ehrenberg, and J. Eckert, *J. Power Sources*, **266**, 198 (2014).
13. M. Schröder, *Chem. Rev.*, **80**, 187 (1980).
14. M. F. Lagadec, M. Ebner, and V. Wood, *Microstructure of Targray PE16A Lithium-Ion Battery Separator*, ETH Zürich (2016).
15. M. Ebner and V. Wood, *J. Electrochem. Soc.*, **162**, A3064 (2015).
16. R. Chandrasekaran, *J. Power Sources*, **262**, 501 (2014).
17. P. Arora, M. Doyle, and R. E. White, *J. Electrochem. Soc.*, **146**, 3543 (1999).
18. J. Cannarella and C. B. Arnold, *J. Electrochem. Soc.*, **162**, A1365 (2015).